JAAS

ROYAL SOCIETY OF CHEMISTRY

COMMUNICATION

View Article Online
View Journal | View Issue

Cite this: J. Anal. At. Spectrom., 2026, 41, 71

Received 16th October 2025
Accepted 27th November 2025

DOI: 10.1039/d5ja00400d

rsc.li/jaas

Recent advances in micro-XANES application in biology at the TwinMic beamline

Valentina Bonanni, *[a] Francesco Guzzi, [a] Milan Žižić, [ab] George Kourousias [a] and Alessandra Gianoncelli [a]

The TwinMic beamline at Elettra synchrotron has been active in the past few decades in research fields such as medicine, pharmacology, toxicology and environmental science, offering combined scanning transmission X-ray and X-ray fluorescence microscopy. Here, we present the recent advances of TwinMic in performing micro X-ray absorption near edge spectroscopy on biological specimens.

Introduction

Soft X-ray microspectroscopy in biology represents a fascinating tool due to its capacity to collect local chemical information with a spatial resolution at the sub-micrometric scale. This can allow discrimination of the various parts of biological systems.

Different components of cells or tissues can play different roles in the function and reaction of cells and organs. They can respond in different ways to external agents like drugs or pollutants, thus the potentiality of selectively discerning which part acts in which way is of crucial importance.[1–4]

X-ray fluorescence (XRF) microscopy is a well-established technique for chemically mapping biological objects with sub-micrometric spatial resolution.[5]

Exciting the atoms of the sample at a specific incident energy enables the detection and localization of several chemical elements whose transition energies of K or L-edges are below the incident energy. Often the technique is performed in raster-scanning mode to reconstruct the elemental maps pixel by pixel, moving the sample across the incident beam. Some synchrotron beamlines combine XRF microscopy with the absorption one in order to simultaneously obtain morphological and chemical information.[6,7]

XRF microscopy aside, the spectroscopic part can be integrated through XANES (X-ray Absorption Near Edge Spectroscopy), recording a stack of images at different incident energies. The main advantage of XANES is the identification of the chemical state of the probed elements whereas XRF microscopy allows identifying the element with no robust hint of its oxidation or bonding condition.[8] XANES detection modes include a variety of options exploiting direct and indirect photons emissions. In the soft X-ray regime, XANES can be collected as the attenuation of the incident beam after the interaction with the sample (transmission mode) or in fluorescence mode, integrating the spectral signal of the emitted photons for all the energies below the excited one.[9] For this last case, the spectroscopic discrimination of the emitted photons is not required, since the energy parameter is determined by the incident beam. The detection can be performed with a photodiode or a photomultiplier, indeed. However, spectral resolution in the XRF detectors is more advisable for discriminating the signal from background or any other noise component. In some cases, the two detection modes, transmission and fluorescence, give similar spectra but the effects of self-absorption have to be considered, particularly in dense samples.

In the soft X-ray regime, where the samples must be thin enough to allow light to be transmitted through the specimens, the XRF signal is expected to show an improved signal to noise level compared to the transmitted one, given that the recorded signal is proportional to the probability of the fluorescence emission and is not directly dependent on the quantity of the transmitted light.

The presented work shows a versatile XANES-based method deployed at the TwinMic beamline of Elettra Sincrotrone Trieste (Trieste, Italy)[10] for achieving more complete spectroscopic characterization of biological samples.

Micro-XANES coupled with Scanning Transmission X-ray Microscopy (STXM) is nowadays a routine technique in several synchrotron beamlines, mainly applied to materials science,[11–14] meteoritics[15] or meteorology[16] and more rarely to biological samples.[17–19]

Most soft X-ray microscopy beamlines have opted for acquiring stacks of images in transmission mode, exploiting the already existing and optimised STXM setup, as it turns out to be the most

[a]Elettra-Sincrotrone Trieste S.C.p.A., Area Science Park Basovizza, 34149 Trieste, Italy. E-mail: valentina.bonanni@elettra.eu

[b]University of Belgrade – Institute for Multidisciplinary Research, National Institute of the Republic of Serbia, 11030 Belgrade, Serbia

rapid acquisition mode. A few beamlines would have the possibility to acquire the spectra in XRF mode, as they also have an integrated XRF detector in the microscope. However, to our knowledge such an option is not exploited. In order to acquire high energy resolution spectra, several XRF maps need to be collected but this acquisition is usually slower than the corresponding STXM images collection, due to the small solid angle acceptance of the XRF detectors and the low XRF yield below 2 keV.

With the current work, we demonstrate the feasibility of both absorption and XRF mode acquisition for XANES soft X-ray measurements in a simultaneous way.

The method here presented has so far been successfully tested only on material science samples at TwinMic. Here, we focused on its implementation on biological samples, whose unordered structures and generally lower concentrations of elements of interest make this application more challenging. As most of the samples investigated at the TwinMic beamline come from the life science field, incorporating such spectroscopy into the already existing imaging techniques will considerably improve the beamline capability, providing more comprehensive information on biological processes.[20,21]

The approach exploits the TwinMic configuration which was conceived for performing STXM and XRF in parallel in the soft X-ray range (400–2200 eV) with a submicrometric spatial resolution.

Stacks of STXM images are collected at different incident energies in the range of a specific absorption edge. In the meantime, also the XRF signal emitted from the excited atoms of the sample is collected. This provides the possibility to process micro-spectra simultaneously collected both in transmission and fluorescence modes.

Two representative cases are shown for this proof of principle investigation: (i) Al K-edge spectra of a soybean (*Glycine max*) root section exposed to Al. Details of previous studies on this sample can be found in ref. 22; (ii) Fe $L_{2,3}$-edges spectra in glioblastoma multiforme (GBM) cells treated with Fe oxide nanoparticles (NPs).[23]

X-rays can damage biological samples during the XANES and/or the XRF acquisition, especially in the soft X-ray regime where the absorption cross section for the light elements is considerably higher compared to the hard X-ray.

The damage process is extremely complex and several aspects can contribute even in an ambiguous way. For instance, the vacuum condition, necessary for performing X-ray analysis in the soft regime, can both reduce the oxidation effect and at the same time can favor the dehydration conditions of the sample.[24]

Even if the damage effect is unavoidable in such a kind of investigation, XANES in itself can help to detect an eventual alteration of the sample condition performing spectrum replicas at different experimental stages. However, even if the spectra are identical, this can also indicate that the changes happened at the beginning of the process and thus, a sample alteration cannot be completely excluded.[2]

Methods

Sample preparation

The details of the preparation of the Al-treated sample are available in the original publication.[22] The sample measured in this study corresponds to a soybean root exposed to 30 μM of $AlCl_3$ for 24 h. A 7 μm thick section was then deposited on a 4 μm thick Ultralene film.

The details of the preparation of the GBM cells exposed to Fe oxide NPs are available in ref. 23.

In particular, for performing the experiment at the TwinMic beamline, the sample was seeded on 200 nm-thick silicon nitride membranes (NanoVision). After 24 h, the membranes were transferred to WillCo dishes and treated with 100 μg mL^{-1} of cell-derived Fe oxide NPs. The sample was fixed with 4% PFA at 4 °C for 20 min, washed twice with Dulbecco's phosphate-buffered saline, and then rinsed twice with water. The sample was then dehydrated before analysis.

STXM and XRF microscopy

The TwinMic setup consists of a STXM microscope where a multilayer Au zone plate of 600 μm of diameter and 50 nm of outermost zone width focalizes the X-ray beam on the sample. The setup is equipped with a double motor system (steppers and piezo-electric) which allows scanning the sample in the plane perpendicular to the incident beam.

The transmitted X-rays are collected with an electron multiplying CCD (EMCCD) camera DV860 from Andor Technology (128 × 128 pixels, 24 × 24 μm^2 pixel size) through an X-ray-visible light converter consisting of a P43 phosphor screen, a lens, a mirror tilted by 45° and an objective lens.

Employing a 2D-type detector instead of a point one allows collecting the differential phase contrast (DPC) signal together with the absorption one.[25,26]

Simultaneously, the XRF photons emitted by the sample are collected by eight silicon drift detectors (SDDs) located symmetrically at 20° from the sample plane. The output signal of the preamplifier electronics (XGLab srl, Bruker Nano-Analytics) is processed through the DANTE Digital Pulse Processor (XGLab srl, Bruker Bruker Nano-Analytics).

A preliminary XRF map was collected on the Al treated specimen. The scanned area is of 40 × 80 μm^2 size, with a stepsize of 0.5 μm (0.69 μm of beam size diameter), with an incident energy of 1.72 keV and a dwell time of 3 s per pixel in order to detect where the Al was mostly localized. The XRF spectra were fitted using PyMCA program.[27]

Then, a sub-area of 10 × 10 μm^2 (same stepsize) was selected to collect a stack of STXM images and XRF maps with a dwell time of 10 ms per pixel and 1 s per pixel, respectively. The incident energy was varied in the range from 1.55 keV to 1.57 keV with a stepsize of 0.25 eV.

A stack of images and maps was collected for a prepared 1μm-thick film of metallic Al standard, under the same experimental conditions. The Al film was deposited through DC magnetron sputtering, using an Al metal target on a Si_3N_4 membrane of 100 nm thickness. The metallic state of the standard was checked by X-ray diffraction and XANES in total electron yield measurements.

Similarly, a preliminary XRF map was collected on the Fe-treated specimen. The scanned area is of 35 × 35 μm^2 size, with a stepsize of 0.5 μm (0.6 μm of beam size diameter), with an

incident energy of 1.5 keV and a dwell time of 2 s per pixel in order to detect where the Fe NPs were mostly localized and to identify the distribution of the elements of the major interest for cells, namely Na and Mg.[28] The XRF spectra were fitted using PyMCA program.

Then, a sub-area of 20 × 20 μm^2 (with the same stepsize) was scanned for collecting a stack of STXM images and XRF maps with a dwell time of 40 ms per pixel and 1 s per pixel, respectively. The incident energy was varied in the range from 0.705 keV to 0.744 keV with a stepsize of 1 eV.

Stack of images and XRF map analysis. The stack of images was pre-processed in several steps. Raw XRF spectra from the eight SDDs were first aligned to a common energy axis and summed to improve the signal-to-noise ratio. Each spectrum was then integrated within a predefined energy window encompassing the expected fluorescence yields. Raw CCD frames were processed separately to extract absorption maps for each energy.

During STXM energy scans, lateral sample shifts were observed, arising not only from thermal drift but also from micro-tilting of the zone plate and changes in focal distance. These effects were partially compensated during acquisition by refocusing along the beam direction and correcting beam displacements in the x and y plane of the sample. Residual misalignments were corrected during data processing using a custom Python pipeline that implements modular subpixel alignment algorithms (phase correlation[29] and SIFT-based[30]). To ensure robustness across datasets, different reference frames (fixed index or previous frame) and contrast modes (absorption, phase, transmission function, or XRF) could be selected. Final absorption and XRF stacks were produced by cropping to the maximum common overlapping region.

The original areas of 10 × 10 μm^2 and 20 × 20 μm^2 have been reduced to 8 × 7 μm^2 and to 14.5 × 15.5 μm^2, respectively, due to the alignment process.

Both of the signals (STXM and XRF) were processed by integrating them for a reduced number of pixels inside and outside of the sample and calculated as:

$$\mu(E) = \ln\frac{I_0}{I};\quad \mu \propto \frac{I_f}{I_0}$$

where μ is the attenuation, E is the incident energy, I_0 is the intensity of the transmitted light through the support, I is the intensity of the transmitted light through the root or the cell and I_f is the intensity of the XRF signal obtained by integrating the counts of the SDD channels.

Spectra were then normalized between 0 and 1 in order to overlap each other for comparison.

Results

Al-treated case

Fig. 1a shows the preliminary Al XRF map performed on the peripheral area of the root section in order to identify the Al accumulation regions. The corresponding STXM image of the same area is shown in Fig. 1b. The energy stack measurements were performed on the bottom right region of the root (red square of Fig. 1a).

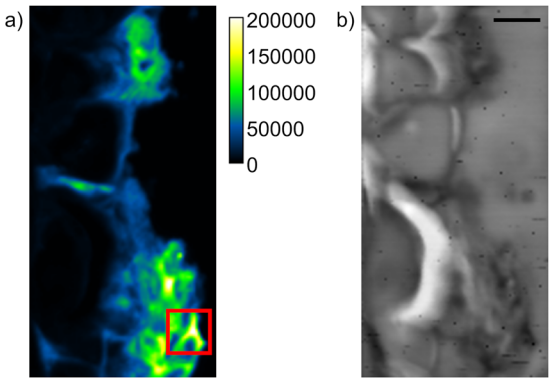

Fig. 1 (a) Al XRF map of the soybean root sample acquired at 1.72 keV, with a stepsize of 0.5 μm (0.69 μm of beam size diameter) and a dwell time of 3 s per pixel. The red square indicates the area selected for the XANES measurements. (b) The corresponding STXM absorption image. The scanned area is 40 × 80 μm^2. The scale bar is 10 μm.

Fig. 2 shows the XANES spectra of a selected subarea of 3 × 3 μm^2 obtained from the stack of the STXM images and from the stack of the XRF signal. In particular, the subregion of 10 × 10 μm^2 was selected from the preliminary scanned area of Fig. 1 due to the high photon counts at the Al K-edge. STXM and the corresponding XRF scans were collected for each incident energy. After the alignment post-processing of the stack of images, the total area was reduced to 8 × 7 μm^2. Spectra were obtained following the procedure explained in the Methods section.

A similar stack of images was acquired for the Al standard sample. Fig. 3 shows the comparison between the spectra of the root sample (acquired in XRF mode) and the Al standard (acquired in transmission mode).

Fe-treated case

The capability of TwinMic to perform XANES experiments on biological systems was tested at the absorption L-edges as well. Fig. 4 shows the preliminary XRF maps of a GBM cell treated

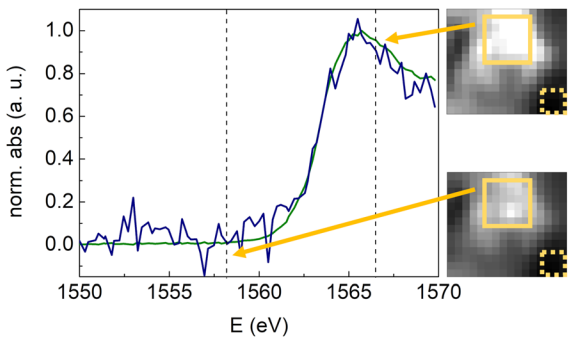

Fig. 2 Al K-edge XANES spectra of a portion of the selected subarea of the soybean root sample acquired as STXM (blue) and XRF (green) signal. The insets show the attenuation in the 8 × 7 μm^2 area at the incident energy of 1566.5 eV (top) and 1558.25 eV (bottom). The yellow squares, respectively 3 × 3 μm^2 and 1.5 × 1.5 μm^2, indicate the portion of the area from which the spectra were integrated (solid line) and the area selected as I_0 (dot line).

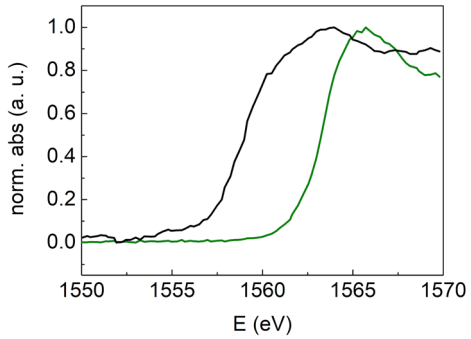

Fig. 3 Al K-edge XANES spectra of the selected subarea of the soybean root sample acquired in XRF mode (green) and of the Al standard acquired in transmission mode (black).

with Fe NPs. Using an incident energy of 1.5 keV allows the simultaneous detection of key endogenous cellular elements such as Na and Mg, along with Fe, which provides insights into the spatial distribution of NPs.

For the energy stack measurements, the central area of the cell of dimension 20 × 20 μm^2 (yellow square in Fig. 4) was selected.

Fig. 5 shows the XANES spectra obtained integrating both the transmission and XRF signals in a subarea of 2 × 2 μm^2.

The I_0 signal was calculated integrating the transmission from a 1 × 1 μm^2 square of the top left corner of the scanned area, where no cell and Fe oxide NPs show a detectable signal.

As in the case of Al K-edge XANES, the spectra were then normalized between 0 and 1 in order to overlap each other for comparison.

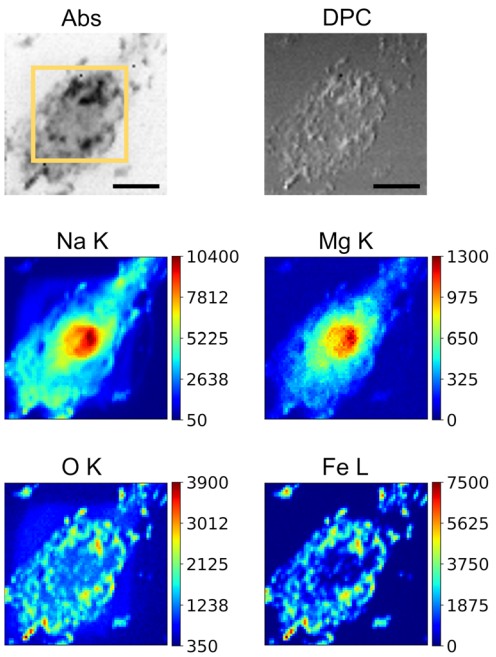

Fig. 4 XRF distribution maps of Na, Mg, O and Fe, shown together with the corresponding absorption (Abs) and differential phase contrast (DPC) STXM images of the GBM cell. The scale bar is 10 μm. The yellow square indicates the area where the XANES stack was measured.

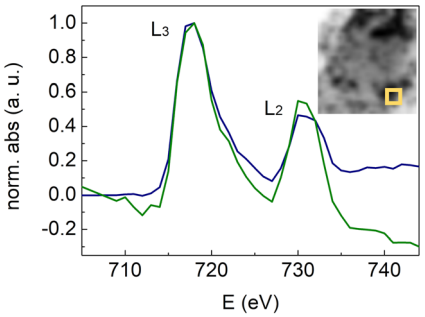

Fig. 5 Fe L-edges XANES spectra of a portion of the selected subarea of GBM cell exposed to Fe oxide NPs acquired in STXM (blue) and XRF (green) mode. The inset shows the attenuation in the 14.5 × 15.5 μm^2 area at the incident energy of 726 eV. The yellow square of 2 × 2 μm^2 indicates the portion of the area from which the spectrum was integrated.

Discussion

Al-treated case

The XRF map of the soybean root sample shows that Al is mainly concentrated in the external root tissues as already reported in ref. 22 and 31. XANES spectra collected in the selected subarea of the root do not show particular differences between the transmission and the fluorescence acquisition modes, except for an expected higher noise level for the former one. The spectral shape recalls what was measured and reported in the literature.[31,32]

Al K-edge is an interesting but extremely complex edge where remarkable shifts in the energy range can be observed passing from the metal to the oxidized state. Apart from energy position, the spectral shape is also extremely complex even for the same oxide, *e.g.*, alumina (Al_2O_3), with different crystal order, *e.g.*, γ-Al_2O_3 and θ-Al_2O_3.[33,34]

In order to verify the energy position of the Al K-edge in these systems compared to metal and alumina samples, measurements were performed under the same experimental conditions, on a metallic Al film (Fig. 3).

The energy position of the Al K-edge indeed appears to confirm the non-metallic state of the Al-treated root.

No additional Al standards could be measured during the experiment. However, the reported results demonstrate the capability of the TwinMic beamline to perform Al K-edge XANES measurements on biological systems and to discriminate between metal and oxide states.

It is important to stress that the XANES micro-spectrum in fluorescence mode shows a signal to noise level comparable to the data obtained on soybean root samples prepared under similar conditions,[32] considering also that in ref. 32 the final spectra were collected on a considerably higher amount of the specimen and as a result of an average of 60 scans from different regions within the same sample.

Fe-treated case

The contrast in the X-ray absorption and DPC images clearly indicates the different density of GBM cell compartments and Fe oxide NPs. The XRF maps of Na and Mg point out the

discrimination between cell nucleus and cytoplasm whereas the O and Fe maps identify the localization of Fe oxide nanoparticles confirming good spatial overlapping between these two elements.

The NPs look mainly localized in the peripheral region. Even if the Fe L-edges XANES signal is detectable in several cell subregions; a representative subarea was selected for showing the spectra measured both in transmission and fluorescence modes. The spectra show the typical Fe $L_{2,3}$ edges shape. The selected energy resolution (1 eV) does not allow for discriminating the spectral shape differences between the metal and the oxide states. However, the results prove the capability of the TwinMic beamline to detect XANES spectra, with a good level of signal to noise, also at a soft X-ray L-edge energy.

Being able to measure XANES at L-edges for transition metals is crucial for several research fields. Compared to K-edges, XANES for the L-orbital symmetry represents a more efficient probe of the coordination of transition metals since any variation is detectable with a better energy resolution and a direct variation in the spectral shape.[35]

Conclusions

Both case studies confirm the feasibility of conducting micro-XANES measurements on biological systems at the TwinMic beamline.

Notably, the multimodal acquisition system of the TwinMic beamline enables the simultaneous collection of micro-XANES spectra in both transmission and fluorescence modes, offering a rare capability worldwide and allowing cross-validation of the results. There are a few other soft X-rays synchrotron beamlines which could use both XANES modes but to our knowledge there is no mention of their simultaneous combination in the literature. Here, we demonstrate the feasibility of such parallel XANES acquisition. With the ongoing upgrade of Elettra 2.0 (ref. 36), both the increased stability and brilliance of the photon source will contribute to further improving TwinMic performances, XANES acquisition capabilities included.

Author contributions

Valentina Bonanni: investigation, formal analysis, visualization, writing – original draft, writing – review & editing; Francesco Guzzi: software, reviewing and editing; Milan Žižić: investigation, reviewing and editing; George Kourousias: software, reviewing and editing; Alessandra Gianoncelli: supervision, reviewing and editing.

Conflicts of interest

There are no conflicts to declare.

Data availability

Data for this article are available at https://vuo.elettra.eu/pls/vuo/open_access_data_portal.show_view_investigation?FRM_ID=60501.

Acknowledgements

The authors are thankful to Prof. Peter Kopittke from Queensland University (Brisbane, Australia) for providing the soybean root sample. The authors are thankful to Dr Simone Dal Zilio (CNR-IOM, Basovizza – Trieste, Italy) for providing the standard Al film. The authors are thankful to Prof. Gianni Ciofani (Center for Materials Interfaces, Electron Crystallography, Istituto Italiano di Tecnologia, Pontedera, Italy), Dr Daniele De Pasquale (IRCSS Ospedale Policlinico San Martino, Genova, Italy), and Dr Carlotta Pucci (The BioRobotics Institute, Scuola Superiore Sant'Anna, Pisa, Italy) for providing the cells treated with Fe NP sample. The authors are thankful to Dr Luca Braglia, Dr Aleksandr Petrov, Hemanita Sharma, Dr Piero Torelli and Dr Giovanni Vinai (CNR-IOM and APE-HE beamlines at Elettra Sincrotrone, Basovizza – Trieste, Italy) for performing total electron yield XANES and X-ray diffraction on the Al standard.

References

1 M. Willans, A. Hollings, R. E. Boseley, T. Munyard, G. C. Ellison and M. J. Hackett, The application of X-ray fluorescence microscopy and micro-XANES spectroscopy to study neuro-metallomics, *J. Inorg. Biochem.*, 2025, **262**, 112744. Available from: https://www.sciencedirect.com/science/article/pii/S0162013424002691.

2 I. J. Pickering and G. N. George, X-Ray Absorption Spectroscopy Imaging of Biological Tissues, *AIP Conf. Proc.*, 2007, **882**(1), 311–315, DOI: 10.1063/1.2644509.

3 R. Ortega, A. Carmona, I. Llorens and P. L. Solari, X-ray absorption spectroscopy of biological samples. A tutorial, *J. Anal. At. Spectrom.*, 2012, **27**(12), 2054–2065, DOI: 10.1039/C2JA30224A.

4 C. Karunakaran, C. R. Christensen, C. Gaillard, R. Lahlali, L. M. Blair, V. Perumal, *et al.*, Introduction of Soft X-Ray Spectromicroscopy as an Advanced Technique for Plant Biopolymers Research, *PLoS One*, 2015, **10**(3), 1–18, DOI: 10.1371/journal.pone.0122959.

5 M. J. Pushie, N. J. Sylvain, H. Hou, M. J. Hackett, M. E. Kelly and S. M. Webb, X-ray fluorescence microscopy methods for biological tissues, *Metallomics*, 2022, **14**(6), mfac032.

6 A. Gianoncelli, G. Kourousias, L. Merolle, M. Altissimo and A. Bianco, Current status of the TwinMic beamline at Elettra: ãsoft X-ray transmission and emission microscopy station, *J. Synchrotron Radiat.*, 2016, **23**(6), 1526–1537, DOI: 10.1107/S1600577516014405.

7 M. K. Abyaneh, T. Araki and B. Kaulich, A Sub-Microanalysis Approach in Chemical Characterisation of Gold Nanorods Formed by a Novel Polymer-Immobilised Gold Seeds Base, *Nanomaterials*, 2017, **7**(10), 331.

8 V. Bonanni and A. Gianoncelli, Soft X-ray Fluorescence and Near-Edge Absorption Microscopy for Investigating Metabolic Features in Biological Systems: A Review [Internet], *Int. J. Mol. Sci.*, 2023, **24**, 3220. Available from: https://www.mdpi.com/1422-0067/24/4/3220.

9 H. A. Castillo-Michel, C. Larue, A. E. Pradas del Real, M. Cotte and G. Sarret, Practical review on the use of

synchrotron based micro- and nano- X-ray fluorescence mapping and X-ray absorption spectroscopy to investigate the interactions between plants and engineered nanomaterials, *Plant Physiol. Biochem.*, 2017, **110**, 13–32. Available from: https://www.sciencedirect.com/science/article/pii/S0981942816302856.

10 A. Gianoncelli, V. Bonanni, G. Gariani, F. Guzzi, L. Pascolo, R. Borghes, *et al.*, Soft X-ray Microscopy Techniques for Medical and Biological Imaging at TwinMic—Elettra, *Appl. Sci.*, 2021, **11**, 7216. Available from: https://www.mdpi.com/2076-3417/11/16/7216.

11 E. B. L. Pedersen, T. Tromholt, M. V. Madsen, A. P. L. Böttiger, M. Weigand, F. C. Krebs, *et al.*, Spatial degradation mapping and component-wise degradation tracking in polymer–fullerene blends, *J. Mater. Chem. C*, 2014, **2**(26), 5176–5182, DOI: 10.1039/C4TC00028E.

12 J. Abed, J. Heras-Domingo, R. Y. Sanspeur, M. Luo, W. Alnoush, D. M. Meira, *et al.*, Pourbaix Machine Learning Framework Identifies Acidic Water Oxidation Catalysts Exhibiting Suppressed Ruthenium Dissolution, *J. Am. Chem. Soc.*, 2024, **146**(23), 15740–15750, DOI: 10.1021/jacs.4c01353.

13 M. Parlinska-Wojtan, T. R. Tarnawski, J. Depciuch, M. L. De Marco, K. Sobczak, K. Matlak, *et al.*, Understanding the Growth of Electrodeposited PtNi Nanoparticle Films Using Correlated In Situ Liquid Cell Transmission Electron Microscopy and Synchrotron Radiation, *Nano Lett.*, 2024, **24**(40), 12361–12367, DOI: 10.1021/acs.nanolett.4c02228.

14 H. J. Nilsson, T. Tyliszczak, R. E. Wilson, L. Werme and D. K. Shuh, Soft X-ray scanning transmission X-ray microscopy (STXM) of actinide particles, *Anal. Bioanal. Chem.*, 2005, **383**(1), 41–47, DOI: 10.1007/s00216-005-3355-5.

15 J. Lier, C. Vollmer, L. Risthaus, D. Kepaptsoglou, Q. M. Ramasse, A. B. Mosberg, *et al.*, The sub-µm petrography of the observed meteorite fall Winchcombe—A complex array of pristine and altered chondrite components, *Meteorit. Planet. Sci.*, 2025, **60**(9), 2149–2165, DOI: 10.1111/maps.70027.

16 C. Pöhlker, K. T. Wiedemann, B. Sinha, M. Shiraiwa, S. S. Gunthe, M. Smith, *et al.*, Biogenic Potassium Salt Particles as Seeds for Secondary Organic Aerosol in the Amazon, *Science*, 2012, **337**(6098), 1075–1078, DOI: 10.1126/science.1223264.

17 A. P. Hitchcock, C. Morin, X. Zhang, T. Araki, J. Dynes, H. Stöver, *et al.*, Soft X-ray spectromicroscopy of biological and synthetic polymer systems, *J. Electron Spectrosc. Relat. Phenom.*, 2005, **144–147**, 259–269.

18 F. Lermyte, J. Everett, J. Brooks, F. Bellingeri, K. Billimoria, P. J. Sadler, *et al.*, Emerging Approaches to Investigate the Influence of Transition Metals in the Proteinopathies, *Cells*, 2019, **8**, 1231.

19 J. Everett, J. Brooks, F. Lermyte, V. T. Tjhin, I. Hands-Portman, E. Hill, *et al.*, Illuminating the brain: Revealing brain biochemistry with synchrotron X-ray spectromicroscopy, *J. Electron Spectrosc. Relat. Phenom.*, 2023, **266**, 147355. Available from: https://www.sciencedirect.com/science/article/pii/S0368204823000725.

20 M. Žižić, M. Stanić, G. Aquilanti, D. Bajuk-Bogdanović, G. Branković, I. Rodić, *et al.*, Biotransformation of selenium in the mycelium of the fungus Phycomyces blakesleeanus, *Anal. Bioanal. Chem.*, 2022, **414**(20), 6213–6222, DOI: 10.1007/s00216-022-04191-4.

21 J. Brooks, J. Everett, F. Lermyte, V. Tjendana Tjhin, P. J. Sadler, N. Telling, *et al.*, Analysis of neuronal iron deposits in Parkinson's disease brain tissue by synchrotron x-ray spectromicroscopy, *J. Trace Elem. Med. Biol.*, 2020, **62**, 126555. Available from: https://www.sciencedirect.com/science/article/pii/S0946672X20301206.

22 P. M. Kopittke, K. L. Moore, E. Lombi, A. Gianoncelli, B. J. Ferguson, F. P. C. Blamey, *et al.*, Identification of the Primary Lesion of Toxic Aluminum in Plant Roots, *Plant Physiol.*, 2015, **167**(4), 1402–1411, DOI: 10.1104/pp.114.253229.

23 D. De Pasquale, C. Pucci, A. Desii, A. Marino, D. Debellis, L. Leoncino, *et al.*, A Novel Patient-Personalized Nanovector Based on Homotypic Recognition and Magnetic Hyperthermia for an Efficient Treatment of Glioblastoma Multiforme, *Adv. Healthcare Mater.*, 2023, **12**(19), 2203120, DOI: 10.1002/adhm.202203120.

24 A. Gianoncelli, L. Vaccari, G. Kourousias, D. Cassese, D. E. Bedolla, S. Kenig, *et al.*, Soft X-Ray Microscopy Radiation Damage On Fixed Cells Investigated With Synchrotron Radiation FTIR Microscopy, *Sci. Rep.*, 2015, **5**, 10250, DOI: 10.1038/srep10250.

25 G. R. Morrison, A. Gianoncelli and B. Kaulich, Image reconstruction using a configurable detector in STXM, *J. Phys.:Conf. Ser.*, 2009, **186**, 012011, DOI: 10.1088/1742-6596/186/1/012011.

26 B. Hornberger, M. D. de Jonge, M. Feser, P. Holl, C. Holzner, C. Jacobsen, *et al.*, Differential phase contrast with a segmented detector in a scanning X-ray microprobe, *J. Synchrotron Radiat.*, 2008, **15**(4), 355–362, DOI: 10.1107/S0909049508008509.

27 V. A. Solé, E. Papillon, M. Cotte, P. Walter and J. Susini, A multiplatform code for the analysis of energy-dispersive X-ray fluorescence spectra, *Spectrochim. Acta Part B At. Spectrosc.*, 2007, **62**(1), 63–68. Available from: https://www.sciencedirect.com/science/article/pii/S0584854706003764.

28 A. Gianoncelli, P. Marmorato, J. Ponti, L. Pascolo, B. Kaulich, C. Uboldi, *et al.*, Interaction of magnetic nanoparticles with U87MG cells studied by synchrotron radiation X-ray fluorescence techniques, *X-Ray Spectrom.*, 2013, **42**(4), 316–320, DOI: 10.1002/xrs.2475.

29 H. Foroosh, J. B. Zerubia and M. Berthod, Extension of phase correlation to subpixel registration, *IEEE Trans. Image Process.*, 2002, **11**(3), 188–200.

30 D. G. Lowe, Object recognition from local scale-invariant features, in *Proceedings of the Seventh IEEE International Conference on Computer Vision*. 1999, vol.2, pp. 1150–1157.

31 P. M. Kopittke, B. A. McKenna, C. Karunakaran, J. J. Dynes, Z. Arthur, A. Gianoncelli, *et al.*, Aluminum Complexation

with Malate within the Root Apoplast Differs between Aluminum Resistant and Sensitive Wheat Lines, *Front. Plant Sci.*, 2017, **8**, 1377, DOI: 10.3389/fpls2017.01377.

32 Z. Li, P. Wang, N. W. Menzies, B. A. McKenna, C. Karunakaran, J. J. Dynes, *et al.*, Examining a synchrotron-based approach for {\it in situ} analyses of Al speciation in plant roots, *J. Synchrotron Radiat.*, 2020, **27**(1), 100–109, DOI: 10.1107/S1600577519014395.

33 B. Akabayov, C. J. Doonan, I. J. Pickering, G. N. George and I. Sagi, Using softer X-ray absorption spectroscopy to probe biological systems, *J. Synchrotron Radiat.*, 2005, **12**(Pt 4), 392–401.

34 Y. Kato, K. Shimizu, N. Matsushita, T. Yoshida, H. Yoshida, A. Satsuma, *et al.*, Quantification of aluminium coordinations in alumina and silica–alumina by Al K-edge XANES, *Phys. Chem. Chem. Phys.*, 2001, **3**(10), 1925–1929, DOI: 10.1039/B100610J.

35 M. L. Baker, M. W. Mara, J. J. Yan, K. O. Hodgson, B. Hedman and E. I. Solomon, K- and L-edge X-ray absorption spectroscopy (XAS) and resonant inelastic X-ray scattering (RIXS) determination of differential orbital covalency (DOC) of transition metal sites, *Coord. Chem. Rev.*, 2017, **345**, 182–208.

36 A. Franciosi and M. Kiskinova, Elettra-Sincrotrone Trieste: present and future, *Eur. Phys. J. Plus*, 2023, **138**(1), 79, DOI: 10.1140/epjp/s13360-023-03654-6.